Supplement to: Phase Resolved Surface Plasmon Interferometry of Graphene

Justin A. Gerber,[1,*] Samuel Berweger*,[1,†] Brian T. O'Callahan,[1] and Markus B. Raschke[1,‡]

[1]*Department of Physics, Department of Chemistry, and JILA, University of Colorado, Boulder, CO 80309, USA*

(Dated: July 1, 2014)

SPP MODEL DESCRIPTION

Here we provide further discussion of the details underlying the model calculations presented in Fig. 4 in the main text. The model describes the observed *s*-SNOM phase and amplitude from graphene Dirac plasmons in terms of the wavelength and damping as they depend on local Fermi energy and carrier mobility.

Fig. S1 shows an expanded version of Fig. 4 in the main text, with a schematic of the cavity model (a). Eq. 2 of the main text describes the SPP response as:

$$\Psi_{gr} = \tilde{\psi}_{gr} + \tilde{\psi}_{SPP,0} + \sum_i \tilde{\psi}_{SPP,i}, \tag{1}$$

where $\tilde{\psi}_{SPP,i} = \tilde{R}_i \times \tilde{\psi}_{SPP,0} \exp\{-2\mathrm{Re}(k_{SPP}) r_i'(\gamma + i)\}$, with SPP wavevector k_{SPP}, a constant term $\tilde{\psi}_{SPP,0}$ describing the local tip-induced SPP, and r_i the distance from tip to the reflecting feature. For all calculations in Fig. S1 we set a normalized amplitude $\tilde{\psi}_{SPP,0} = 1$ that can be scaled to agree with experimental results. We chose the reflection coefficient $\tilde{R} = -1$ in agreement with the experimentally observed reflection conditions. In the following, and for illustration purposes only we choose $\gamma = 0.1$ (i.e.,

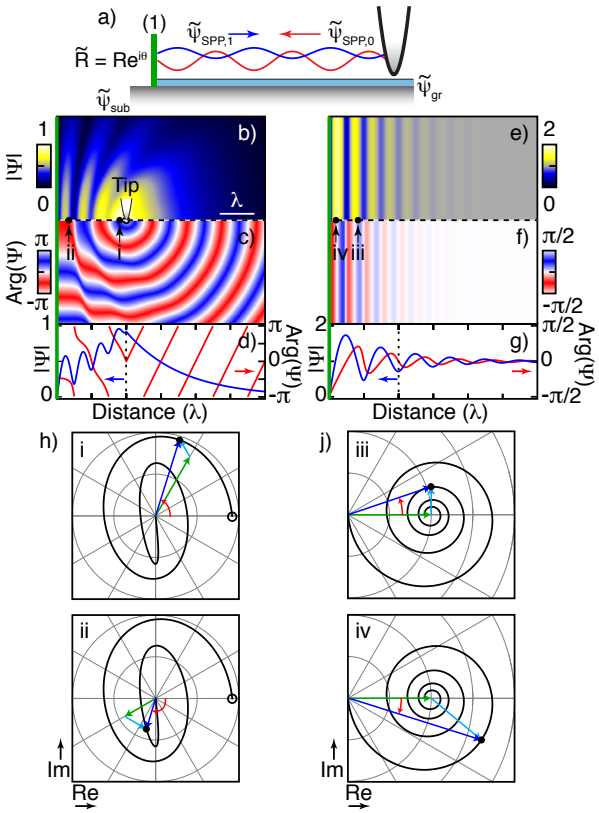

FIG. S1: Illustration of graphene SPP cavity model (a). Calculated standing SPP distribution of amplitude (b), phase (c), and corresponding line cut (d) along the center line, with local excitation by a stationary tip and reflection from a boundary at left edge. Resulting spatial standing wave SPP map of *s*-SNOM amplitude (d), phase (e), and corresponding line cut (f) when scanning the tip. Phase-space plots (h) and (j) of line cuts from region between left boundary and dashed line in (d) and (g), respectively, with phasors as indicated for selected points (see text for further details).

smaller than what is observed experimentally) to better demonstrate the underlying propagation-induced interference effects. We furthermore set the dielectric term $\tilde{\psi}_{gr} = 0$ as this only provides a SiO_2 substrate-induced offset.

Eq.1 assumes SPP source and probe to be located at the same spatial location in accordance with experimental tip-scanning conditions. However, to illustrate the underlying instantaneous spatial distribution of the SPP wave away from the tip we generalize Eq. 1

$$\Psi_{gr} = \tilde{\psi}_{gr} + \tilde{\psi}'_{SPP,0} + \sum_i \tilde{\psi}'_{SPP,i} \tag{2}$$

in order to account for the *propagation* of the launched SPP away from the tip by including a spatially varying term $\tilde{\psi}'_{SPP,0} = \tilde{\psi}_{SPP,0} \exp\{-\mathrm{Re}(k_{SPP}) r'_0(\gamma - i)\}$ with r_0 the distance from the tip. Similarly, we account for the modified geometry with $\tilde{\psi}'_{SPP,i} = \tilde{R}_i \times \tilde{\psi}_{SPP,0} \exp\{-\mathrm{Re}(k_{SPP}) r'_i(\gamma + i)\}$ with the net propagation distance r'_i of the reflected SPP (assuming geometric reflection). We note that under experimental conditions where $r_0 = 0$ and $r'_i = 2r_i$, Eq. 2 reduces to Eq. 1.

Using Eq 2, the resulting spatial SPP distribution is shown in Fig. S1 with amplitude (b), and phase (c), as induced by a stationary point source (tip) at a fixed distance from a reflecting straight boundary located on the left edge (green line). A line cut of phase and amplitude along the dashed line separating (b) and (c) is shown in (d). Due to the propagation-indued spatial evolution of $\tilde{\psi}'_{SPP,0}$, the SPP phase increases linearly with distance from the tip as seen in (d) and is only weakly modulated by the reflected wave. As a result, the period of the amplitude oscillation as seen in (b) is $\lambda/2$. While the phase (c) exhibits an apparent periodicity of λ, we note that the modulation due to the reflected wave has a period of $\lambda/2$.

We then model the experimental tip scanning conditions using Eq. 1. Scanning the tip results in a *standing* wave pattern with the amplitude shown in (e), phase (f), and corresponding line cut (g). Both amplitude and phase exhibit a periodicity of $\lambda/2$.

In order to further illustrate the nature of the SPP interference, in Fig. S1(h) and (j) (black lines), we show a complex plane representation of the region of the line cuts in (d) and (g) between the reflecting boundary and dashed lines, respectively. The open circle in (h) shows the position of the tip, with the boundary location corresponding to the center. Phasors for selected points i and ii are shown as indicated. Green arrows represent $\tilde{\psi}'_{SPP,0}$ and turquoise arrows $\tilde{\psi}'_{SPP,1}$, which sum to give $|\Psi|$ (blue arrows) and $\mathrm{Arg}(\Psi)$ (red arrows). In the absence of the reflected wave, the black curve would follow an ideal counterclockwise spiral due to $\tilde{\psi}'_{SPP,0}$. The ellipticity is due to the superposition of $\tilde{\psi}'_{SPP,1}$, which rotates in a clockwise direction due to the opposite direction of propagation.

In contrast, for the case of *s*-SNOM scanning, panel (j) shows the standing wave spp evolution between the reflecting boundary and the position indicated by the dashed line in (g). The start of the spiral, with coordinate origin at the left edge of graph, corresponds to the position at the reflecting boundary. Phasors for selected points are iii and iv are shown as indicated. Green arrows show $\tilde{\psi}_{SPP,0}$ and turquoise arrows show $\tilde{\psi}_{SPP,1}$, which, as above, sum to give $|\Psi|$ (blue arrows) and $\mathrm{Arg}(\Psi)$ (red arrows). With $\tilde{\psi}_{SPP,0}$ independent of tip position, the green phasors remain stationary at 1, while the turquoise phasor rotates in a clockwise direction, resulting in a spiral offset by $\tilde{\psi}_{SPP,0}$ and thus centered at 1. Note that two rotations of the spiral correspond to translation by a single wavelength, giving rise to the $\lambda/2$ period of the oscillations. The spiral centered at $\tilde{\psi}_{SPP,0} = 1$ also explains the $\sim 90^\circ$ phase difference between the amplitude and phase: The amplitude exhibits a maximum when $\tilde{\psi}_{SPP,0}$ and $\tilde{\psi}_{SPP,1}$ sum in a parallel direction at the equilibrium value of $\mathrm{Arg}(\Psi) = 0$ and the phase is maximum near the equilibrium value of $|\Psi| = 1$.

DEFECT SCATTERING

Here we describe additional measurements showing the scattering of a graphene SPP from a small defect. Shown in Fig. S2(a) is the AFM topography with the corresponding near-field amplitude (b) and phase (c). In the topography a surface contaminant of unknown origin is seen with a diameter of $\sim$100 nm. In both the amplitude and phase the contaminant is seen to act as a scatterer with an SPP interference pattern seen to emit radially.

Several notable things are seen in the SPP interference pattern, shown clearly in a line cut (d) taken from the dashed lines in (b) and (c). First, the interference amplitude is seen to decrease above the defect. This arises due to the increased tip-graphene separation reducing the strength of the near-field interaction, resulting in a decreased scattering intensity as well as SPP launching efficiency. This effect is further magnified through possible screening by the dielectric contaminant. However, unlike the amplitude, the phase does show a clearly visible SPP oscillation. This underscores the robustness of the phase signal.

Along with the decrease in SPP amplitude, the SPP wavelength is seen to decrease. This is likely the result of the inverse relation between λ_{SPP} and κ. Here the presence of the dielectric on the graphene in place of air increases κ and thus decreases the SPP wavelength. Due to the gradual nature of the change in κ we have not been able to adequately model this feature.

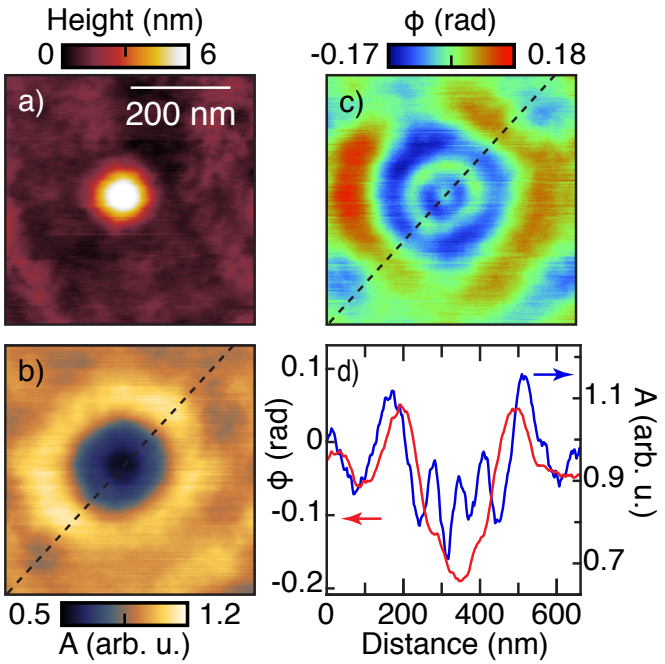

FIG. S2: AFM topography (a) and corresponding near-field amplitude (b) and phase (c). Line cut (d) taken along the dashed lines in (b) and (c).

BILAYER WAVELENGTH

For the bilayer, an estimate of λ_{SPP} [1, 2], using otherwise identical parameters, predicts twice the SPP wavelength of single layer graphene, thus exceeding the experimental wavelength by a factor of 2.5. This indicates an unusually large reduction in the Fermi level of that bilayer segment.

* These authors contributed equally to this work.
† Current address: National Institute of Standards and Technology, Boulder, CO, 80305
‡ Electronic address: markus.raschke@colorado.edu

[1] R. Roldán and L. Brey, Phys. Rev. B **88**, 115420 (2013).
[2] R. Sensarma, E. H. Hwang, and S. Das Sarma, Phys. Rev. B **82**, 195428 (2010).